

Full Length Article

Tuning oxygen vacancies and resistive switching properties in ultra-thin HfO₂ RRAM via TiN bottom electrode and interface engineering

Zhihua Yong ^{a,1}, Karl-Magnus Persson ^{b,1}, Mamidala Saketh Ram ^b, Giulio D'Acunto ^a, Yi Liu ^a, Sandra Benter ^a, Jisheng Pan ^c, Zheshen Li ^d, Mattias Borg ^b, Anders Mikkelsen ^a, Lars-Erik Wernersson ^{b,*}, Rainer Timm ^{a,*}

^a Division of Synchrotron Radiation Research, Department of Physics, and NanoLund, Lund University, Box 118, Lund 221 00, Sweden

^b Department of Electrical and Information Technology, Lund University, Box 118, Lund 221 00, Sweden

^c Institute of Materials Research and Engineering, A*STAR (Agency for Science, Technology and Research), 2 Fusionopolis Way, Innovis, #08-03, Singapore 138634, Singapore

^d Department of Physics and Astronomy, Centre for Storage Ring Facilities (ISA), Aarhus, Denmark

ARTICLE INFO

ABSTRACT

Keywords:

RRAM
Resistive switching
Hafnium oxide
Titanium nitride
X-ray photoelectron spectroscopy
Band bending

Resistive random access memory (RRAM) technologies based on non-volatile resistive filament redox switching oxides have the potential of drastically improving the performance of future mass-storage solutions. However, the physico-chemical properties of the TiN bottom metal electrode (BME) can significantly alter the resistive switching (RS) behavior of the oxygen-vacancy RRAM devices, yet the correlation between RS and the physico-chemical properties of TiN and HfO_x/TiN interface remains unclear. Here, we establish this particular correlation via detailed material and electrical characterization for the purpose of achieving further performance enhancement of the stack integration. Two types of RRAM stacks were fabricated where the TiN BME was fabricated by physical vapor deposition (PVD) and atomic layer deposition (ALD), respectively. The HfO_x layer in HfO_x/PVD-TiN is more oxygen deficient than that of the HfO_x/ALD-TiN because of more defective PVD-TiN and probably because pristine ALD-TiN has a thicker TiO₂ overlayer. Higher concentration of oxygen vacancies induces a larger magnitude of band bending at the HfO_x/PVD-TiN interface and leads to the formation of a higher Schottky barrier. Pulsed endurance measurements of up to 10⁶ switches, with 10 μA ± 1.0 V pulses, demonstrate the potential of the studied ultra-thin-HfO_x/TiN device stack for dense, large scale, and low-power memory integration.

1. Introduction

New paradigms in computing, such as memory-centric computation, machine learning, and big data analytics, have moved the computational bottleneck away from the number of floating point computations per second to the size, bandwidth, and energy consumption of the memory. To address this bottleneck, non-volatile resistive memory technologies are currently being researched with the potential to deliver fast, low power, and high cost efficiency memory solutions. One interesting candidate for resistive switching is oxygen-vacancy resistive random access memory (OxRRAM). Due to its low complexity material stack, potential for high density 3D integration, low current and low voltage operation, and 5 ns pulsed programming capability, it could

target ultra-low power, high speed, and mass-storage solutions [1–4].

One of the more challenging aspects of OxRRAM, as compared to other resistive memory technologies, is the switching endurance where values are typically reported in the range of 10⁵–10¹² switching cycles [5–7]. To improve the endurance, a lower oxygen vacancy concentration at the bottom metal electrode (BME) interface is beneficial, and choosing a more inert metal may improve the endurance. As such, the intricate details of the metal deposition and post-treatment are of high importance. However, there is currently a lack of studies that cover both the electrical properties as well as detailed interface and material characterization of devices implementing a scaled switching oxide and that is operated in a low-current regime. The differentiation of high performance devices from those with significantly worse switching

* Corresponding authors.

E-mail addresses: lars-erik.wernersson@eit.lth.se (L.-E. Wernersson), rainer.timm@sljus.lu.se (R. Timm).

¹ These authors contributed equally to this work.

behaviour is to a large degree due to intricate differences of the material interfaces, and a relevant question is to what extent the specific properties of the ideally non-participating bottom electrode matter in respect of the performance. Typically, the switching behavior of the RRAM is related to the size of the filament, where more stable switching can be achieved with a larger filament and higher currents. Nevertheless, for ultra-dense and large scale integration beyond scaled oxides, the maximum current switching level needs to be kept to around $10 \mu\text{A}$ to match the conduction of ultra-scaled selectors, and thus, for relevant studies, the filament size needs to match that requirement. This paper aims at providing a thorough study on how to optimize the switching oxide/BME interface for electrical operation in line with the conductance limitations of scaled selectors.

TiN is commonly used by the industry due to its Si-Complementary-Metal-Oxide-Semiconductor (Si-CMOS) compatibility, having a relatively large work function, being relatively inert, and that it can be selectively etched. Although it is generally accepted that TiN could act as an oxygen reservoir and that oxidation of the TiN BME could strongly modify the switching behavior of the OxRRAM devices [8,9], the correlations between the physico-chemical properties of HfO_x and TiN BME and the subsequent resistive switching properties are still not fully clear. We therefore seek to learn more about the pristine HfO_x/TiN interface and the surface of the TiN BME to identify how the different fabrication procedures affect the material quality and correlate them with the subsequent OxRRAM switching properties. To investigate this, both electrical measurements and X-ray photoelectron spectroscopy (XPS) were performed. XPS was deployed as it is well-known as a powerful non-destructive tool to study the elemental composition and the physico-chemical properties of material surfaces [10,11]. Since synchrotron radiation-based XPS allows a wide range of tuneable excitation energies, this enables the inelastic mean free path (λ) of the excited electrons and thus the probing depth to be varied, hence allowing both the surface sensitive studies of the HfO_x top layer to be performed at lower energy [11], as well as the more bulk sensitive physico-chemical analysis of the interface of the HfO_x/TiN heterostructure to be conducted at higher energy [10–12].

In this work, two types of OxRRAM stacks were fabricated, consisting of a titanium nitride (TiN) BME, a hafnium oxide (HfO_x) switching oxide layer, and an indium-tin-oxide (ITO) top metal electrode (TME), and where the two types only differ by the fabrication procedures of the TiN BME, using either physical vapor deposition (PVD) or atomic layer deposition (ALD). Electrical characterization shows that the resistive switching of PVD-TiN devices has a larger spread between switching cycles of both the resistance values and the required switching voltages. ALD-TiN devices, on the other hand, exhibit significantly reduced switching distributions and lower probability of an oxide breakdown. The differences in the oxidation of the TiN BME in the two types of HfO_x /

TiN stacks are evaluated using XPS and are correlated with the crystallite size of the dominant (111) 20 plane peak of cubic TiN, which is obtained using X-ray diffraction (XRD). From the synchrotron radiation-based X-ray photoemission spectroscopy (SXPS) studies, we find that the HfO_x layer in $\text{HfO}_x/\text{PVD-TiN}$ is more oxygen deficient than that of $\text{HfO}_x/\text{ALD-TiN}$. We also demonstrate that the difference in the magnitude of the band bending of the energy bands in the HfO_x layer is attributed to the difference in the extent of O^{2-} interstitial scavenging from the HfO_x layer by the TiN BME in the two types of OxRRAM stacks. Modelling of electrical characterization suggests the presence of a Schottky barrier at the HfO_x/TiN interface. The difference in Schottky barrier height, in combination with the larger base size of the conductive filament for the PVD-TiN, is likely to explain the discrepancy in the switching distributions between the two samples. The ALD-TiN OxRRAM with 3.3-nm-thick HfO_x shows promising performance with intact low voltage switching up to 10^6 switches. By understanding how the different fabrication steps affect the oxide interface/BME as laid out in this study, and correlating them with the oxygen vacancy concentration, it is possible to optimize the stack integration for improved performance. With our demonstration of an ultra-scaled switching oxide that has the capability of both low current and low-voltage switching, in combination with an in-depth understanding of the physico-chemical properties at the materials interface, the studied OxRRAM stack has the potential to target future ultra-dense, large scale, and low-power memory solutions.

2. Experimental methods

The OxRRAM device samples were fabricated on a Si-substrate covered with a 200-nm-thick thermal oxide for device isolation. Additional samples optimized for XPS characterization were fabricated on a p-doped Si-substrate, with a native SiO_2 layer of about 1.3 nm thickness, for high substrate conductivity. All the samples were fabricated together during the deposition of the BME and the HfO_x . The samples used for electrical measurements will be termed as the TiN devices whereas those used for XPS will be labelled as either TiN or HfO_x/TiN samples. A cross-sectional SEM image, as well as schematic images of one of the electrically characterized OxRRAM devices, is shown in Fig. 1. The PVD-TiN BME was deposited using sputtering at room temperature with a TiN target and a power of 150 W in an Ar ambient with a flow of 9 sccm. The ALD-TiN was deposited at 250 °C using a tetrakisdimethylamido-titanium (TDMA-Ti) precursor and a 300 W N_2 -plasma with 5 min /cycle. The resistivities of the two films are determined to be $2.7 \cdot 10^{-6} \Omega\text{m}$ and $1.6 \cdot 10^{-5} \Omega\text{m}$ for the PVD- and ALD-TiN, respectively. For the device samples, the BME was etched out using a SF_6/N_2 -plasma after deposition, where the BME area was contacted in later processing steps using two different vias. Next, a 3.3 nm thick HfO_2 layer was deposited on all samples except the TiN reference samples at 200 °C using a

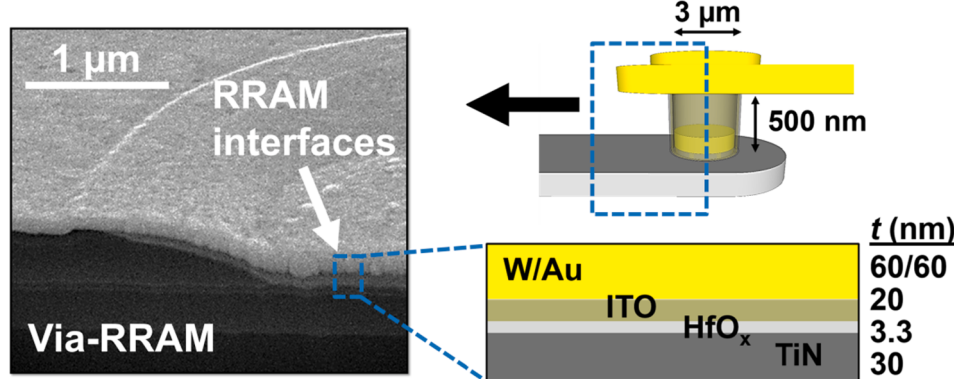


Fig. 1. A cross-sectional SEM image and schematics show the implemented OxRRAM via structure as well as the different materials in the OxRRAM-stack. The etched-out TiN BME is contacted through an organic lifting layer using vias, where a smaller 3 μm wide optical-lithography-defined via is the active OxRRAM. The thickness t of the OxRRAM material layers is indicated.

tetrakisethylmethylenamido-hafnium (TEMA-Hf) precursor and a 40 sccm O₂-flow with a 300 W O₂-plasma for durations of 80 s/cycle. Subsequently, the TiN and HfO_x/TiN samples were transferred to the ultra-high vacuum (UHV) chambers of the XPS and SXPS setups, while the device samples were finalized as follows: An organic spacer was spin-coated and baked at 200 °C to separate the probing pads from the substrate, and vias to the BME were patterned with UV-lithography. The ITO TME was deposited in a separate step using sputtering of an ITO target with 50 W RF power in an Ar ambient with a 9 sccm flow. The ITO was confined to a 6 μm disc that covered the 3 μm resistive random access memory (RRAM) via opening using a Cl/Ar-dry-etch. Before doing the final metallization of sputtered W and Au, the HfO_x in the BME contact opening was removed using a hydrogen fluoride wet-etch.

The electrical characterization was performed with an Agilent B1500 parameter analyzer, where WGMUs pulse generators were used to perform pulsed measurements. In order to enforce a strict current compliance, an external discrete component Metal-Oxide-Semiconductor-Field-Effect-Transistor (MOSFET) was connected in series in a 1-transistor-1-RRAM circuit configuration (1T1R).

Conventional XPS spectra were obtained using a Thermo Fisher Scientific Theta Probe system equipped with a monochromatic, micro-focused Al Ka (1486.6 eV) X-ray source and a hemispherical electron energy analyzer. A low-energy electron flood gun was used for compensation of sample charging. The C 1 s peak from adventitious carbon at 284.6 eV was used as a reference for charge correction. Analysis chamber base pressure was 5×10^{-10} mbar under ultra-high vacuum (UHV) condition. In addition, SXPS in UHV was performed at the HIPPIE undulator beamline of the MAX IV Laboratory in Lund, Sweden. The beamline delivers a photon flux of $> 10^{12}$ photons/s, and an energy range of 270 eV – 2200 eV is available. The analyzer used is Scienta Hipp-3 with SWIFT acceleration mode. The base pressure of the analysis chamber was about 5×10^{-9} mbar. More details of the HIPPIE

beamline and its endstation have been reported elsewhere [13]. All binding energies (BE) were calibrated with respect to the Au 4f_{7/2} core level BE of a reference gold sample. Furthermore, SXPS investigations were also performed at the Material Science Beamline (AU-MATLINE) located in the Aarhus University synchrotron facility, ASTRID2. The usable energy range is from 20 eV – 1000 eV. The beamline is equipped with a SCIENTA SES200 electron energy analyzer and a SX-700 monochromator. The base pressure of the analysis chamber was around 5×10^{-10} mbar under UHV condition. Hf 4f spectra were fitted by Gaussian-Lorentzian (G-L) functions with Shirley-type background subtraction; the Gaussian full width of half maximum (FWHM) was kept free during fitting while the Lorentzian FWHM was constrained at 0.1 eV [11]. The spin-orbit splitting was fixed at 1.66 eV[11] and the branching ratio of Hf_{7/2} peak to Hf_{5/2} peak was kept to 1.33.

The surface morphology of the TiN and the HfO_x films was studied by atomic force microscopy (AFM) with a Bruker Dimension Icon 300 microscope. The Dimension Icon AFM was operated in Peak Force Tapping mode by employing Sb n-doped Si cantilevers (Bruker RTESPA-300) with a nominal force constant of 40 Nm⁻¹ and resonance frequency of 300 kHz. The crystal structures of the TiN/Si and HfO_x/TiN/Si samples were investigated using the Cu K α 1 radiation of a STOE Stadi-MP powder diffractometer.

3. Results and discussions

Our results are presented in five sub-sections, manifesting the interplay of electrical and structural characterization. We start Section 3.1 by discussing results from the electrical measurements regarding filament forming, reverse filament forming and RRAM switching characteristics of the devices with PVD-TiN and ALD-TiN BMEs. The XPS, SXPS XRD and AFM characterization and data analysis of the TiN layers in the reference TiN samples, as well as the interface in the HfO_x/TiN

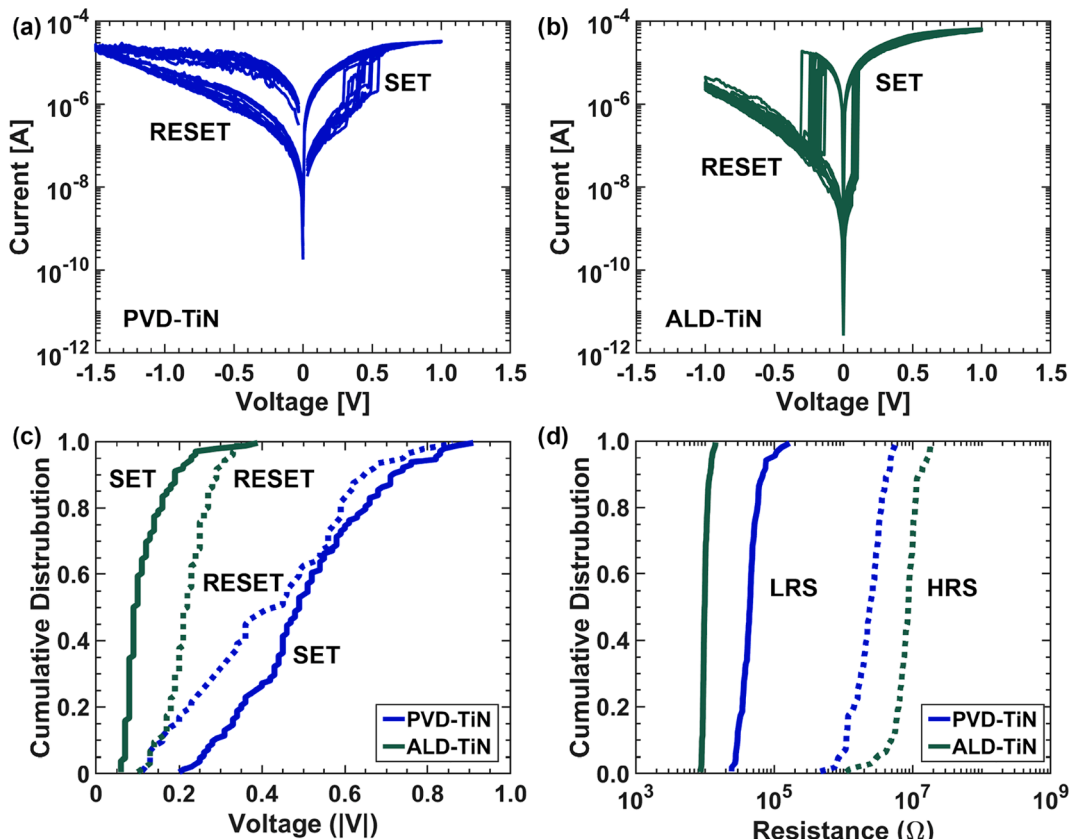


Fig. 2. Switching characteristics for (a) a PVD-TiN and (b) an ALD-TiN OxRRAM for 20 consecutive DC sweep cycles. Comparison of the cumulative distributions of (c) the absolute value of the switching voltages and (d) the resistance states for 120 continuous cycles for PVD-TiN and ALD-TiN OxRRAM cells.

samples, are covered in [Section 3.2](#), while the SXPS studies of the HfO_x layer of the HfO_x/TiN samples are described and elaborated in detail in [Section 3.3](#). After understanding the physico-chemical properties of the BME and the material interface, we return to the electrical device performance: Temperature dependent electrical measurements and the conduction behaviour analysis of the TiN devices are reported in [Section 3.4](#). Finally, the pulsed endurance of the TiN devices is evaluated in [Section 3.5](#).

3.1. RRAM switching characteristics

We start by comparing the key performance of the RRAM devices, i.e. the DC switching characteristics, of our PVD- and ALD-TiN OxRRAM memory cells, as shown in [Fig. 2a](#) and [2b](#), respectively. The only difference between the two cells is the processing of the TiN BME. Once an oxygen vacancy filament has been formed in the OxRRAM by applying a large positive voltage (V_{FORM}) at the TME, the resistance can be modulated between a high resistive state (HRS) and a low resistive state (LRS) by locally rupturing the filament tip with a negative TME voltage, referred to as a RESET, and then reforming it with a positive TME voltage, referred to as a SET. V_{RESET} and V_{SET} are the voltages required to cause a RESET and SET, respectively, and are typically significantly smaller than V_{FORM} . To maximally extend the OxRRAM switching endurance, parasitic formation of oxygen vacancies throughout the switching oxide should be minimized by proper selection of material combinations. One common source of switching failure is when a back-forming occurs during a RESET, where the ruptured oxygen vacancy

filament is reformed by vacancies supplied by the bottom metal electrode (BME). This is referred to as a reverse filament formation (RFF), widely studied in the literature [\[14–16\]](#).

The cumulative distributions of V_{SET} and V_{RESET} for 120 consecutive switching cycles, as well as the LRS and HRS, are shown in [Fig. 2c](#) and [2d](#), respectively. A cumulative distribution is a set of data that has been sorted from the smallest to the largest value and that is plotted against a y-axis that typically goes from 0 to 1, representing a probability from 0 to 100% that a certain parameter is within a specific interval. This type of plot gives a good visualization of the mean and variance of each dataset and contrasts them across all the collected data. The distribution of the switching data is narrower for the ALD-TiN device, within ± 0.4 V, whereas the characterization of the PVD-TiN device shows larger voltage spreads of ± 0.9 V. The switching voltage is here defined as the specific voltage when the applied voltage divided by the measured current corresponds to the resistance at the maximum positive or negative applied voltage. The memory window is also significantly larger for the ALD-TiN device with an average of 860x versus 50x for the PVD-TiN device, with the resistance measured at a TME voltage of -50 mV.

When referring to filament size, it is important to distinguish between the width of the narrowest section that will limit the LRS-level, and the widths of the base at the BME and TME oxide-interfaces that impact the HRS-level as well as the probability for backforming. For a relevant study, it is important that the OxRRAM is operated at a conductance level compatible with scaled selectors at about 10 μA , limiting the width of the most resistive section of the conductive

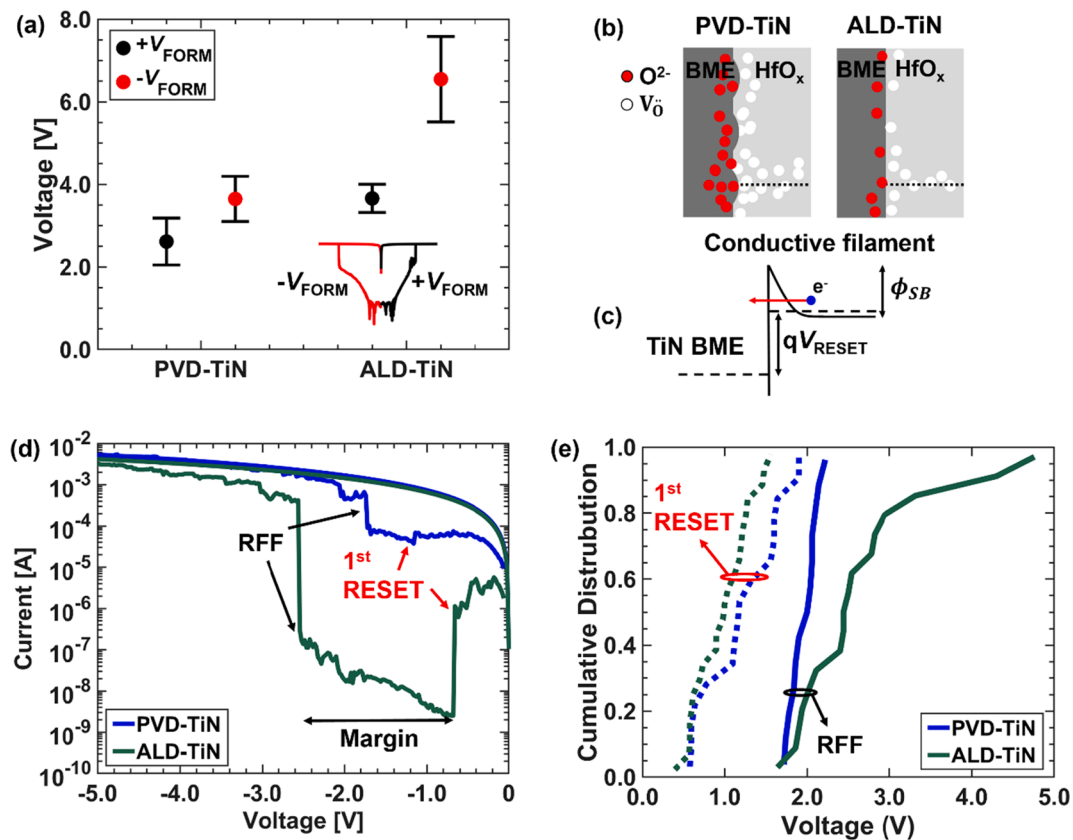


Fig. 3. (a) Forming voltage distributions in the positive ($+V_{\text{FORM}}$) and the negative ($-V_{\text{FORM}}$) bias direction. The inset shows forming sweeps for $+V_{\text{FORM}}$ and $-V_{\text{FORM}}$ for a PVD-TiN device. (b) Schematic illustrations of the TiN BME and HfO_x interface for both the PVD-TiN and ALD-TiN where the red and white circles refer to doubly negatively charged oxygen ions and doubly positively charged oxygen vacancies, respectively. The dotted lines indicate the positions of the conductive filaments. (c) The conduction band profile of the formed filament at the proximity of HfO_x/TiN interface with an applied bias V_{RESET} during filament rupture, where a Schottky barrier, ϕ_{SB} , is present at the interface. (d) The 1st RESET that is swept up to a large negative voltage for both the PVD-TiN and ALD-TiN devices. (e) Comparison of the cumulative distributions of the voltage for the 1st RESET and the RFF. (For interpretation of the references to colour in this figure legend, the reader is referred to the web version of this article.)

filament. The filament tends to be thicker at the material interfaces, forming cone shaped bases, as the oxygen vacancy concentration is higher than in the middle of the switching oxide. Regarding the base of the filament at the BME-oxide-interface, it is important that it is kept at a minimum to hinder unwanted leakage in the HRS and to lower the probability for backforming that would leave the device in a permanent LRS. As seen in the Fig. 2a and 2b, the ALD-TiN device has an abrupt SET and RESET, while the PVD-TiN device has a more gradual RESET and SET. Monte Carlo simulations of RRAM filaments show that a thicker base at the BME interface tends to have a gradual switching as the filament is progressively reduced, and that a slightly higher initial defect density near the BME is enough to cause a filament base widening [17]. A larger filament base for PVD-TiN device also explains the reduced memory window as compared to the ALD-TiN device due to the larger area of the ruptured filament surfaces. Restive switching is to varying degrees dependent on both the critical field and the amount of Joule heating that is induced by an applied voltage. For low current, low voltage switching RRAM, the voltage required to accomplish DC switching is foremost dependent on the vacancy formation energy at the TME/oxide interface [18]. A barrier at the TME interface will increase the required V_{SET} while a barrier at the BME interface will increase the V_{RESET} . It is difficult to differentiate how the different sizes and shapes of the filaments and the difference in barrier height at the BME interface affect the switching. However, as both SET and RESET are affected similarly, the barrier difference is likely secondary to the filament size difference.

To further quantify the difference between the two samples, electrical characterization of the filament formation and initial rupture was performed. In Fig. 3a, V_{FORM} for both positive ($+V_{FORM}$) and negative ($-V_{FORM}$) TME bias are shown. The mean of the data of the PVD-TiN devices displays both smaller $+V_{FORM}$, 2.6 V versus 3.7 V for ALD-TiN devices, and smaller $-V_{FORM}$, 3.6 V versus 6.5 V for ALD-TiN devices. The difference in forming voltages can be explained by a higher concentration of oxygen vacancies at the BME interface for the PVD-TiN sample, effectively reducing the gap to be bridged for a positive filament formation.

Schematic images of the interfaces for the two different samples are shown in Fig. 3b. The conduction band with an arbitrary Schottky barrier height at the BME interface in the filament during rupture is displayed in Fig. 3c. For a negative forming, the BME reservoir drastically reduces the needed bias as it can supply vacancies without the need of vacancy formation. In Fig. 3d, characteristics of the 1st RESET and the subsequent RFF are plotted for both PVD-TiN and ALD-TiN devices. In Fig. 3e, the cumulative distributions of both types are shown. The measured data included in Fig. 3a, 3d, and 3e is shown in Fig. S1 in the Supplementary Material (SM). Typically, the 1st RESET is larger than the RESET voltage required after a few switches due to an overshoot during forming, and thus it is critical not to reach an RFF failure at this initial step when switching with a large negative voltage. It can be noted that the margin between the 1st RESET and the RFF is larger for the ALD-TiN device as the distribution for V_{RESET} is smaller and the distribution for the RFF voltage is higher. IV conduction mode fittings and analysis for PVD-TiN and ALD-TiN devices are discussed in the latter Section 3.4. To identify and understand the underlying factors leading to the observed differences in the electrical behaviour, XPS measurements of the TiN layer and the BME interface were performed and will be discussed in the next few sections.

3.2. Oxidation and characterization of TiN layers

We start our investigation of the physico-chemical properties by analyzing the surface of TiN reference samples, consisting of TiN layers on a Si substrate, since this TiN surface is the starting point for the latter formation of the HfO_x/TiN BME interface. After deposition by either PVD or ALD, the TiN reference samples were exposed to air before XPS measurements were carried out. Ti 2p core-level XPS spectra for both the

PVD-TiN and the ALD-TiN layers are shown in Fig. 4a. The Ti 2p spectra constitute the main components of Ti 2p ($2p_{3/2}$ and $2p_{1/2}$) doublet peaks of TiO_2 [19], satellite peaks of TiN, TiO_yN_z and TiN [20,21], in the order of decreasing BE, as observed in the inset of the fitted Ti 2p spectra in Fig. 4a. TiO_2 is the dominating component in the spectra for both reference samples, confirming the strong oxidation of the TiN layer that was expected, according to the discussion of the oxidation mechanism that occurred in the TiN layer as described in the Supplementary Material. From Fig. 4a, it was further observed that the ALD-TiN layer has more TiO_2 on its surface, as compared to PVD-TiN. Since both samples had been exposed to air for the same time, the thicker TiO_2 overlayer formed atop the ALD-TiN indicates that this TiN layer was already oxidized to a larger degree upon the deposition process. This can be well explained by the facts that 1) the ALD-TiN was deposited at 250 °C at base vacuum pressure of 10^{-5} mbar whereas the PVD-TiN was deposited at room temperature at base vacuum pressure of 3×10^{-7} mbar and 2) more oxygen residue gas is found in the ALD chamber since O_2 plasma is often utilized while the sputtering chamber is not connected to any oxygen supply outlet. The increased presence of residual oxygen at elevated temperature favors TiN oxidation, as discussed in more detail below. Additionally, the surface of ALD-TiN also seems to have more TiO_yN_z than that of PVD-TiN, as seen in Fig. 4a. These observations are further verified in the N 1s spectra of the ALD-TiN and PVD-TiN (SM Fig. S2), which show that the surface of ALD-TiN has slightly more titanium oxynitride than PVD-TiN.

To further understand the crystal structure of the TiN reference samples, XRD was performed and the results were plotted in Fig. 4b. The presence of the peaks in the powder XRD spectra which are related to the TiN, TiO_2 and TiO_yN_z implies that these compounds are all polycrystalline under the current fabrication conditions. The XRD spectra of both samples contain the (023) crystal plane for orthorhombic titanium oxynitride and the (111) and (222) crystal planes for cubic TiN. Only the ALD-TiN possesses the (210) crystal plane for rutile TiO_2 , which corroborates the thicker overlayer of TiO_2 on the ALD-TiN as seen in the XPS results in Fig. 4a. The inset in Fig. 4b depicts the magnified dominant cubic-TiN (111) 20 plane peak of the reference TiN samples. According to the Scherrer formula, a larger FWHM of the TiN (111) peak of the PVD-TiN implies smaller crystallite size and thus more grain boundaries, which in turn increase the number of shortcut diffusion paths for oxidation to occur [22,23]. A larger FWHM also implies that the PVD-TiN is subjected to more micro-strain as compared to the ALD-TiN due to larger extent of non-uniform lattice distortion or more lattice dislocation.

The morphology differences are further highlighted by atomic force microscopy (AFM) images, as shown in Fig. 4c for PVD- and ALD-TiN. The PVD-TiN film has a significantly smaller grain size of about 60 nm^2 in average than the ALD-TiN that has a corresponding value of 200 nm^2 , which is consistent with the XRD results. The root-mean-square surface roughness values are 10.0 Å and 3.0 Å for PVD- and ALD-TiN, respectively. These in fact should result in more oxidation in the PVD-TiN since lower crystal quality will lead to easier surface oxidation by providing more diffusion pathways. However, this was not observed in the XPS results from the reference samples because the rate of oxygen diffusion across the oxide overlayer is the rate-limiting step in oxidation kinetics [24–26] and this diffusion process is dependent on the deposition temperature [25–27]. According to Eq. (S1) in the Supplementary Material, the rate of oxidation of ALD-TiN is higher than PVD-TiN as ALD-TiN was deposited at a much higher temperature than PVD-TiN. Therefore, the oxygen ions would receive more energy from the ALD-TiN, increasing both their surface diffusion length as well as their probability to overcome the activation barrier to diffuse across the TiO_2 overlayer and into the ALD-TiN for oxidation to occur. This effect seems to have dominated over the larger number of diffusion paths in the PVD-TiN and have resulted in a thicker TiO_2 overlayer atop ALD-TiN.

Turning now to the HfO_x/TiN samples, we want to reveal how the differences between the PVD- and ALD-TiN BMEs influence the HfO_x

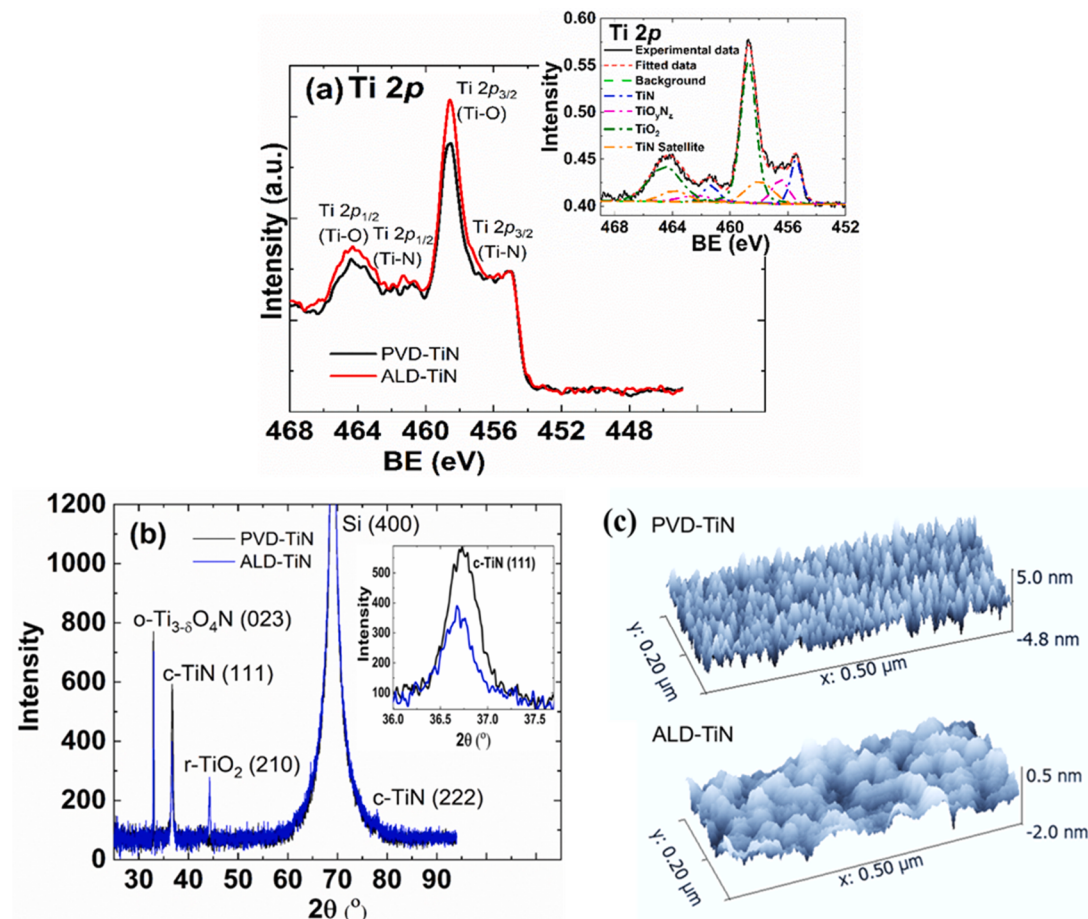


Fig. 4. (a) Ti 2p XPS spectra of the PVD- and ALD-TiN reference samples, taken using a monochromatic Al K α X-ray source. Inset shows a typical fitted Ti 2p spectrum of TiN, showing the different components in the spectrum. (b) XRD spectra of the PVD-TiN and ALD-TiN samples [o: orthorhombic, c: cubic and r: rutile]. Inset shows the magnified dominant (1 1 1) 2 θ plane peak of cubic-TiN. The FWHM of c-TiN (1 1 1) 2 θ plane peak of PVD-TiN is larger than that of ALD-TiN. (c) AFM images of the PVD- and ALD-TiN samples; PVD-TiN has a smaller grain size than ALD-TiN.

deposited on top. In order to evaluate the physico-chemical properties of the HfO_x/TiN samples at different depth, SXPS was performed at the HIPPIE beamline of the Max IV laboratory and Ti 2p, N 1 s, Hf 4f, and O 1 s spectra of the HfO_x/TiN samples were collected at different photon energies of 1250 eV, 1750 eV and 2063 eV. These photon energies correspond to inelastic mean free paths which limit our depth of

information mainly to the HfO_x layer ($h\nu = 1250$ eV), increase it to the HfO_x/TiN interface ($h\nu = 1750$ eV), or extend it further into the TiN layer ($h\nu = 2063$ eV). The Ti 2p SXPS results were plotted in Fig. 5a and 5b for the HfO_x/PVD-TiN and HfO_x/ALD-TiN samples, respectively. Generally, the Ti-O peaks are more pronounced in the spectra taken with lower photon energy, while the intensity of the Ti-N peaks increases

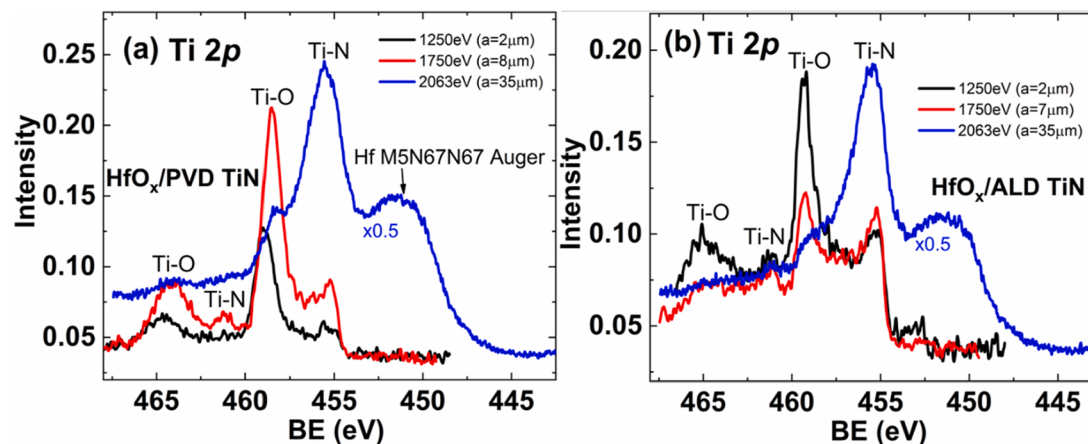


Fig. 5. Ti 2p SXPS spectra of (a) HfO_x/PVD-TiN and (b) HfO_x/ALD-TiN samples taken at photon energies of $h\nu = 1250$ eV, 1750 eV and 2063 eV. The “a” value in the parenthesis refers to the slit width used during data collection. A larger slit width will result in higher intensity in the SXPS measurement at a specific photon energy, but also in larger energy broadening. At $h\nu = 2063$ eV, a Hf Auger peak is overlapping with the low BE range of the Ti 2p core level.

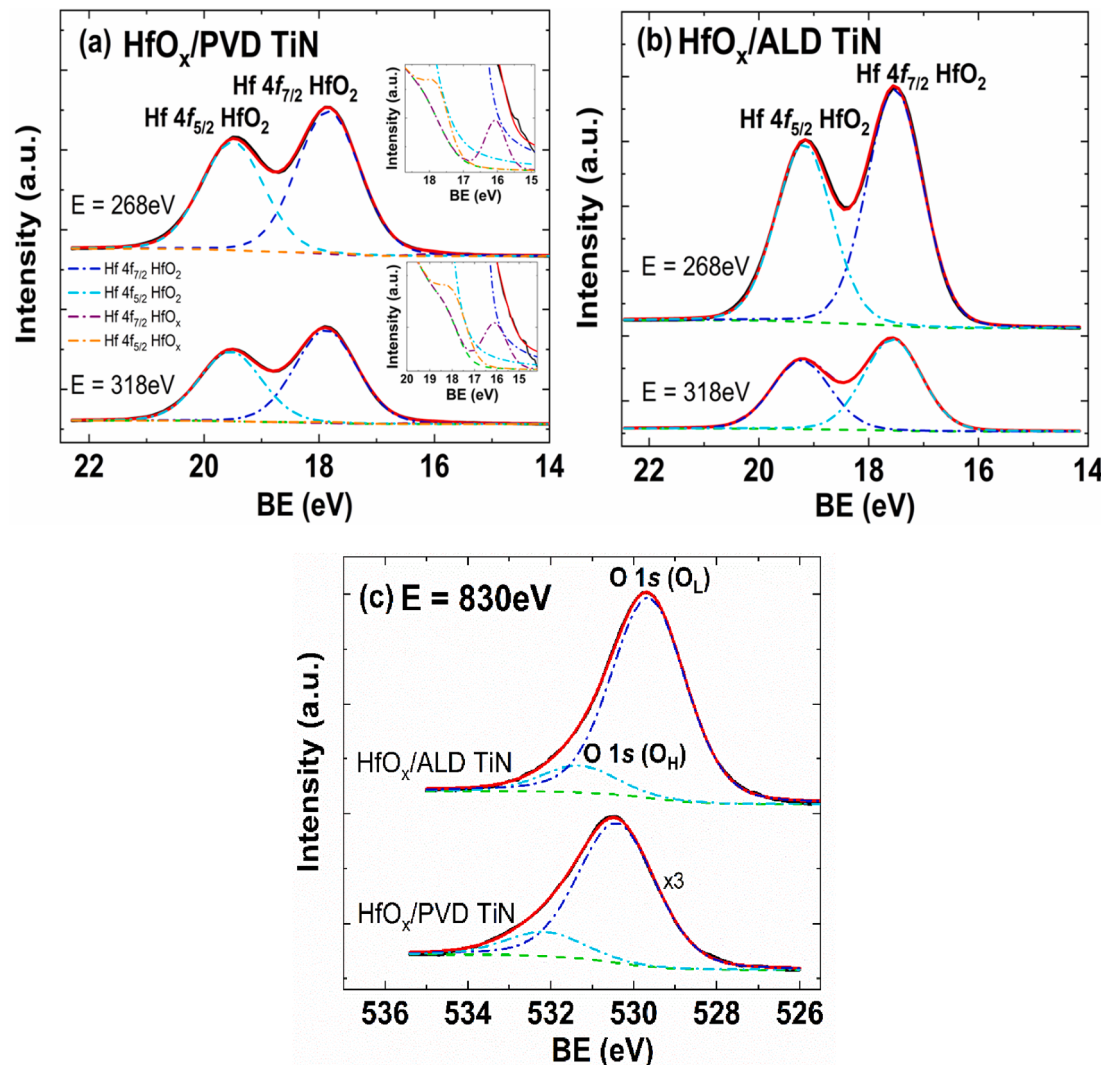


Fig. 6. Fitted Hf 4f SXPS spectra of (a) HfO_x/PVD-TiN and (b) HfO_x/ALD-TiN samples taken at $\hbar\nu = 268$ eV and 318 eV. Insets in (a) display the magnified oxygen-deficient hafnium sub-species located at lower BE in the spectra of the HfO_x/PVD-TiN. (c) Fitted O 1 s SXPS spectra of HfO_x/ALD-TiN (top) and HfO_x/PVD-TiN (bottom) samples taken at $\hbar\nu = 830$ eV. Fitted Hf 4f and O 1 s components are indicated; the green dashed line denotes the fitted Shirley background. (For interpretation of the references to colour in this figure legend, the reader is referred to the web version of this article.)

with increasing photon energy, indicating that TiO₂ has formed on top of the TiN layer, as one could expect. At $\hbar\nu = 1750$ eV, which corresponds to the case where the detection of the HfO_x/TiN interface region ($\lambda \approx 3.3$ nm) is most sensitive, the Ti-O/Ti-N ratio is higher for the HfO_x/PVD-TiN sample than for the HfO_x/ALD-TiN sample. This implies that the TiO₂ layer formed at the HfO_x/PVD-TiN interface is now thicker than that of the HfO_x/ALD-TiN interface. This suggests that after ALD deposition of HfO₂ at 200 °C, the PVD-TiN layer not only reacted with oxygen plasma in the ALD chamber but most likely also scavenged a lot of oxygen from the HfO_x interface region to form TiO₂ and TiO_yN_z. This can be explained by the fact that there are more grain boundaries and higher defect concentration in the PVD-TiN than in the ALD-TiN, as verified by the XRD results in Fig. 4c, which help to pave the way for more oxidation to occur. The morphology of the TiN layer should, from an electrical standpoint, primarily affect the forming voltage as a larger TiN layer roughness may lead to larger variations in the deposited oxide film thickness. Once the filament is formed, however, the roughness should be less significant as the switching will occur at the same location where a portion of the formed filament is ruptured and reformed. One report [28], however, found that increased surface roughness reduced the mean and the spread of the RRAM switching voltages, speculated to be due to more focused electrical fields at sharp positions.

Interestingly, we also noticed a decrease in thickness of the interfacial TiO₂ layer in the HfO_x/ALD-TiN sample, when compared to the TiO₂ overlayer on the pristine ALD-TiN reference sample. This is deduced by comparing the peak height ratio of Ti-O to Ti-N in the Ti 2p spectra of HfO_x/ALD-TiN measured at $\hbar\nu = 1750$ eV (Fig. 5b) to that of the pristine ALD-TiN (Fig. 4a). Reduction in the thickness of both TiO₂ and TiON layers after ALD of 3 nm HfO₂ top layer has also been reported by Egorov *et al* [29] and they attributed this to the heating of the sample up to $T = 240$ °C in the low pressure (~1 mbar) N₂ atmosphere. However, we think that in this case, self-cleaning effect of native oxide (TiO₂) during dosing of the TEMA-Hf precursor in HfO₂ ALD on TiN, similar to self-cleaning of native oxides on semiconductors upon HfO₂ ALD [10,30], is most probably the main reason. This will be further explained and elaborated in the discussions of Hf 4f and O 1 s spectra in Fig. 7.

The N 1 s SXPS results were plotted in SM Figs. S3a and S3b for the HfO_x/PVD-TiN and HfO_x/ALD-TiN samples, respectively. The peak area ratio of TiO_yN_z to TiN is higher for the HfO_x/ALD-TiN sample, as compared to HfO_x/PVD-TiN. This suggests that HfO_x/ALD-TiN contains more titanium oxynitride than HfO_x/PVD-TiN and implies that the likelihood of formation of large amounts of oxynitride at the interface of the HfO_x/PVD-TiN is not high.

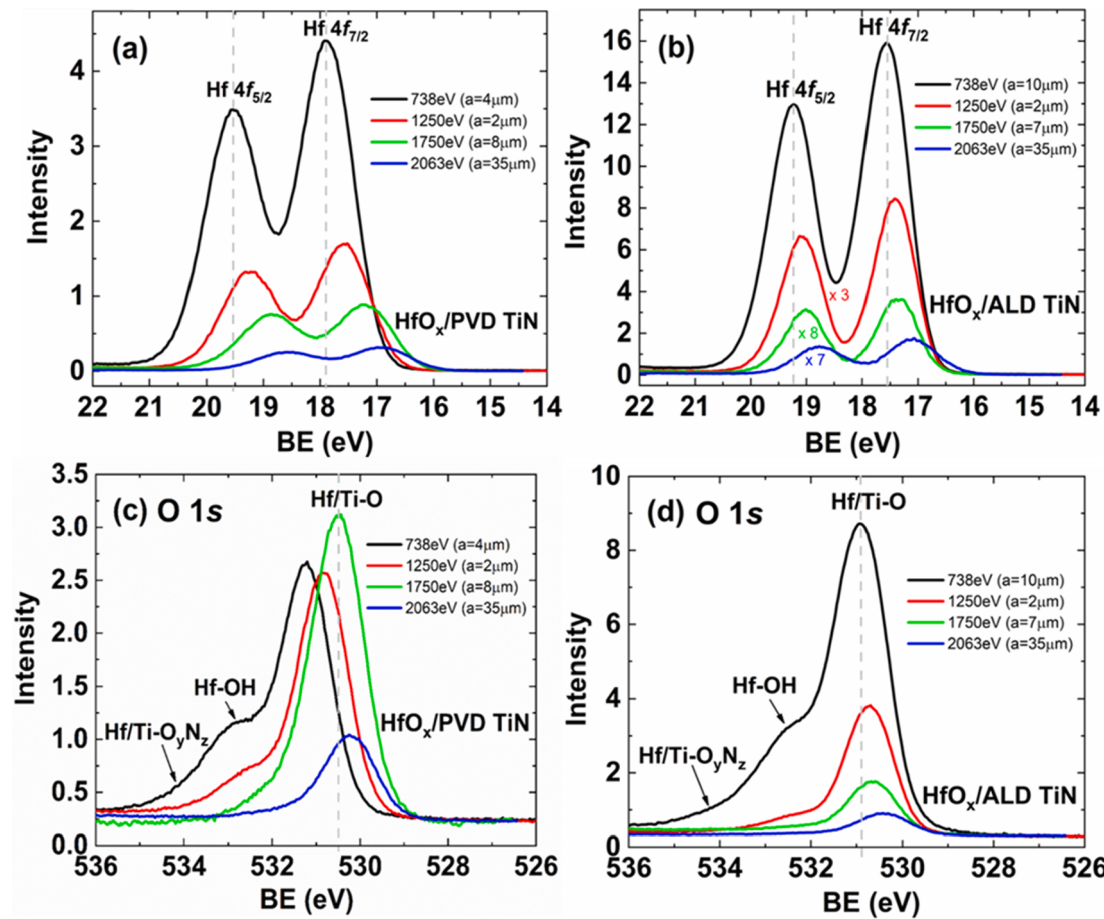


Fig. 7. Hf 4f SXPS spectra of (a) HfO_x/PVD-TiN and (b) HfO_x/ALD-TiN samples taken at $\hbar\nu = 738$ eV, 1250 eV, 1750 eV and 2063 eV. O 1 s SXPS spectra of (c) HfO_x/PVD-TiN and (d) HfO_x/ALD-TiN samples taken at $\hbar\nu = 738$ eV, 1250 eV, 1750 eV and 2063 eV. All SXPS spectra were collected at the HIPPIE beamline of the MAX IV Laboratory. The “a” value in the parenthesis refers to the slit width used during data collection. A larger slit width will result in higher intensity in the SXPS measurement at a specific photon energy, but also in larger energy broadening.

3.3. XPS characterization of HfO_x

To evaluate the elemental composition of hafnium and oxygen in the HfO_x layers and to reduce the signal from the TiO₂ interfacial layer, additional Hf 4f and O 1 s SXPS measurements were performed at the Au-Matline beamline of the ASTRID2 synchrotron, which is more suitable for lower photon energy acquisition. The SXPS data collected at lower photon energies will be much more surface sensitive than those collected at the HIPPIE beamline. Fig. 6a – b exhibit the fitted Hf 4f SXPS data.

As seen in Fig. 6a and 6b, the Hf 4f spectra of the HfO_x/PVD-TiN sample can be fitted by two doublets whereas only one doublet is needed to fit the Hf 4f spectra of the HfO_x/ALD-TiN sample. The extra component at lower BE needed to fit the HfO_x/PVD-TiN spectra can be attributed to non-stoichiometric hafnium oxide. This signifies that there are more oxygen-deficient hafnium sub-species in the HfO_x layer of HfO_x/PVD-TiN, as compared to the one in HfO_x/ALD-TiN.

Fig. 6c shows the O 1 s spectra which were fitted using G-L mix functions, with Lorentzian FWHM constrained at 0.38 eV, after an iterated Shirley-type background subtraction. The O 1 s spectra of both samples can be de-convoluted into two peaks: a well-formed peak at lower BE and a small shoulder at higher BE. The peak at lower BE can be ascribed to the O²⁻ ion under fully oxidized stoichiometric conditions – oxygen (O_L) in HfO₂ lattice, while the shoulder peak at higher BE is attributed to the bridging hydroxyls (O_H). The fitted results were summarized in Table 1. From the area under the curve of the fitted spectral components, the empirical ratio O/Hf was obtained, defined as the ratio

Table 1

SXPS analysis data for calculation of the apparent ratio O/Hf (area ratio of O1s: Hf 4f_{7/2} peaks). Error bar of XPS core level spectra is within ± 0.05 eV.

| Sample ID | BE (Hf 4f _{7/2}) [eV] $\hbar\nu = 318$ eV | FWHM (Hf 4f _{7/2}) [eV] | BE (O 1 s (O _L)) [eV] $\hbar\nu = 830$ eV | FWHM (O 1 s (O _L)) [eV] | Ratio O/Hf |
|---------------------------|---|-----------------------------------|---|-------------------------------------|------------|
| HfO _x /ALD-TiN | 17.57 | 1.24 | 529.64 | 2.11 | 0.186 |
| HfO _x /PVD-TiN | 17.88 (16.10) ^a | 1.28 (1.28) ^a | 530.41 | 2.20 | 0.174 |

^a Refers to the oxygen deficient Hf sub-species.

between the O1s and Hf 4f_{7/2} peak areas. Only a comparison of the relative values is meaningful here since different pass energies were used during O1s and Hf 4f spectral acquisition. This ratio is found to be lower for the HfO_x layer of HfO_x/PVD-TiN, implying it to be more oxygen deficient in the bulk than the HfO_x layer of HfO_x/ALD-TiN. These results are consistent with the electrical measurements as shown in Fig. 3a, where both the + V_{FORM} and the -V_{FORM} are smaller for the PVD-TiN device due to higher concentration of oxygen vacancies at its BME interface, as compared to the ALD-TiN device. The reasons pertaining to the differences in the oxygen deficiency level of the HfO_x layers of HfO_x/TiN will be discussed in detail in Fig. 7. From Fig. S4 and Table S1 in the SM, both the HfO_x layers of HfO_x/PVD-TiN and HfO_x/ALD-TiN samples are also verified to be oxygen richer on the surface than in the bulk. The

HfO_x layer of $\text{HfO}_x/\text{PVD-TiN}$ is also probably more defective since it has more hydroxyl groups (SM Table S2) attached to the surface, as compared to the one in $\text{HfO}_x/\text{ALD-TiN}$.

In order to understand how the oxidation of TiN affects the elemental composition of HfO_x and finally the electrical performance of the OxR-RAM memory cells, we utilized the SXPS photon energies suitable for probing through the top HfO_x layer to the HfO_x/TiN interface and discuss the Hf 4f spectra (Fig. 7a and 7b) and the O 1 s spectra (Fig. 7c and 7d) obtained at different photon energies. All the Hf 4f spectra consist of one Hf 4f doublet component of HfO_x , whereas the O 1 s spectra comprise of three features which are associated with the O 1 s peaks of 1) HfO_2 or TiO_2 , 2) bridging hydroxyls connected to Hf and 3) HfO_yN_z or TiO_yN_z , listed in ascending BE.

From Fig. 7, we made two important observations. Firstly, the BE of Hf 4f and O 1 s peaks shift in the same direction with increase in photon energies. Secondly, both the Hf 4f doublet peaks and the O 1 s peaks of the HfO_x/TiN samples progressively shift to lower BE with increase in photon energies which correspond to a larger X-ray penetration depth in the samples. However, we find that these shifts are less pronounced in both the Hf 4f and O 1 s spectra of the $\text{HfO}_x/\text{ALD-TiN}$ sample, as compared to the corresponding spectra of the $\text{HfO}_x/\text{PVD-TiN}$ sample.

In both HfO_x/TiN samples, the Hf 4f spectra in Fig. 7a - b and the O 1 s spectra in Fig. 7c and 7d are observed to progressively shift to lower BE with increase in photon energies. Conversely, the Ti 2p and N 1 s spectra in Fig. 5 which were measured at the same photon energies as the Hf 4f and O 1 s spectra for the same samples did not exhibit a BE shift. This evinces that the BE downshifts in the Hf 4f and O 1 s spectra are not caused by experimental artifacts, such as sample charging. Often in XPS, a shift in BE is due to different chemical composition at different depth. However, if the measured BE shifts were related to a depth-dependent change in the Hf-O composition, there would be a change in the Madelung potential or the valence number and charge transfer would have happened between the Hf^{4+} and the O^{2-} ions, then the resultant BE shift in the Hf 4f and O 1 s spectra should have opposite sign [31]. In contrary, the trend of Hf 4f and O 1 s BE shift with increase in photon energy are in the same direction, which instead reveals a change in the Fermi level (E_F) in the HfO_x film, implying that the spectral shift of O 1 s cannot be interpreted as a composition change [31,32].

To explain the BE downshift trend of Hf 4f and O 1 s and to understand the reason that leads to the magnitude differences of the BE shifts in the Hf 4f and O 1 s spectra of the HfO_x/TiN samples, we first investigated the crystal structures of both samples. For this purpose, XRD reference samples were fabricated under the same parameters as the samples optimized for XPS, but with ~ 15 nm thick HfO_x films. No crystal phase related to HfO_2 was detected in the XRD spectra of both the ~ 15 nm $\text{HfO}_x/\text{ALD-TiN}$ and $\text{HfO}_x/\text{PVD-TiN}$ samples (SM Fig. S5). The AFM image of HfO_x (SM Fig. S6) shows a relatively flat surface; these all verified the amorphous nature of HfO_x . Since oxygen interstitial ions are abundant in the amorphous HfO_x/TiN samples, this renders the scavenging of oxygen from amorphous HfO_x to form an interfacial TiO_2 layer highly plausible. Although the oxygen affinity of HfO_2 is higher than that of TiN and the Gibbs free energy of formation of HfO_2 is more negative than that of TiO_2 and TiN [33], density functional theory (DFT) calculations performed using the projector augmented wave (PAW) method have revealed that the small conduction band offset of TiN in HfO_2/TiN might lead to the formation of doubly negatively charged oxygen interstitials and these charged interstitials have a low activation barrier to diffusion through the HfO_2 layer [34]. These results suggest that at high oxygen concentration, O^{2-} interstitial ions will accumulate at the HfO_2/TiN interface and if N vacancies are available, the O^{2-} -interstitial ions will diffuse into TiN and the probability of inward diffusion of O^{2-} ions will be higher for defective TiN layers [34]. Thus, the differences between the magnitude of the BE shift in the Hf 4f and O 1 s spectra of the $\text{HfO}_x/\text{PVD-TiN}$ and $\text{HfO}_x/\text{ALD-TiN}$ samples are most likely ascribed to the difference in the extent of O^{2-} interstitial diffusion into the TiN BME.

The BE downshift trend of Hf 4f and O 1 s in the same direction with increase in photon energies can then be explained by the generation of positively charged oxygen vacancies in the dielectric HfO_x layer after the N vacancies in TiN scavenged negatively charged oxygen interstitials [34–36] from it, which follows the reaction [36,37]: $\text{O}_o^{2-} - 2e = V_O + 2e + \text{O}_M$ where O_o^{2-} refers to doubly negatively charged oxygen interstitial, V_O corresponds to doubly positively charged oxygen vacancies, e is an electron and O_M is assigned to an oxygen atom that either diffused into the TiN electrode, where it might have oxidized a Ti atom, or released into the atmosphere as a molecule. At the same time, equal negative charges were also built up on the TiN side after it absorbed the doubly negatively charged oxygen interstitials [38,39]. The flow of the O^{2-} interstitials will continue until the E_F of TiN and HfO_x are aligned. Since charges cannot accumulate locally in metal, the transferred electrons were therefore distributed uniformly at the TiN interface and hence, no space charge region was formed in TiN. This in turn created a space charge region with excess positive charges in the HfO_x layer close to the material interface which acts as the depletion layer. An internal non-uniform electric field⁴² was thus built up within the space charge region in HfO_x and subsequently, band bending occurred and the energy bands of the HfO_x layer bent upward, leading to the downshift of O 1 s and Hf 4f peaks to lower BE as shown in Fig. 7a – d. Band bending has also been previously reported in the $\text{HfO}_2/\text{SiO}_2/\text{Si}$ system [31,37,40,41]. The amount of band bending is largest close to the HfO_x/TiN interface and decreases through the HfO_x layer towards the surface. Accordingly, the shifts of the Hf 4f and O 1 s peaks towards lower BE get larger with increasing probing depth.

The general relationship among the magnitude of band bending (E_{bb}) near the metal–semiconductor junction, the depletion width (z_d) and the density of the negatively charged oxygen interstitials (N_d) that diffused into TiN can be represented by Eqs. (1) and (2) below. N_d is also equivalent to the density of the positively charged oxygen vacancies (P_d) generated in the HfO_x layer after the oxygen interstitials diffused into the TiN layer. Derivation of the equations and approximations, as well as the assumptions made for the model which explain quantitative differences from experimental results, are found in the SM.

The band bending difference at any position z in the depletion layer is given by:

$$E_{bb} = \frac{N_d}{\epsilon} ze^2 \left(z_d - \frac{1}{2} z \right)$$

When $z = z_d$,

$$E_{bb} = \frac{N_d e^2 z_d^2}{2\epsilon} \quad (1)$$

$$N_d = \frac{2eE_{bb}}{e^2 z_d^2} = P_d \quad (2)$$

where ϵ is the permittivity of the HfO_x .

The SXPS results for the estimation of magnitude of band bending (E_{bb}) were tabulated in Table 2. It is noticed that the BE downshift values

Table 2

SXPS analysis data for the estimation of magnitude of band bending (E_{bb}). The change in BE (ΔBE) at the specified photon energy is calculated by subtracting the BE value at the specified photon energy from the BE measured at $\hbar\nu = 2063$ eV. Error bar of XPS core level spectra is within ± 0.05 eV.

| Sample ID | BE (Hf 4f _{7/2}) [eV] | ΔBE (Hf 4f _{7/2}) [eV] | ΔBE (Hf 4f _{7/2}) [eV] | BE (O 1 s) [eV] | ΔBE (O 1 s) [eV] | ΔBE (O 1 s) [eV] |
|-------------------------------|---------------------------------|--|--|-----------------|--------------------------|--------------------------|
| $\text{HfO}_x/\text{ALD-TiN}$ | 17.08 | 0.48 | 0.35 | 530.43 | 0.50 | 0.27 |
| $\text{HfO}_x/\text{PVD-TiN}$ | 16.98 | 0.93 | 0.6 | 530.26 | 1.00 | 0.59 |

*The ΔBE values ($\hbar\nu = 1750$ eV) are excluded because $\lambda \geq 3.3$ nm and there is no big difference between these values obtained for both samples.

for both Hf $4f_{7/2}$ and O 1 s with respect to photon energy of 2063 eV for $\text{HfO}_x/\text{PVD-TiN}$ are about twice the corresponding values for $\text{HfO}_x/\text{ALD-TiN}$. From Table S3 in the SM, nearly the same amount of BE shifts is observed for the Hf $4f_{7/2}$ ($\hbar\nu = 1250$ eV) and O 1 s ($\hbar\nu = 1750$ eV) peaks for respective HfO_x/TiN sample when both the photon energies of 1250 eV for Hf 4f and 1750 eV for O 1 s yield $\lambda \approx 3.3$ nm; the reference baseline BE are selected at photon energies of 738 eV for Hf 4f and 1250 eV for O 1 s where $\lambda \approx 2.2$ nm in both cases. The larger extent of the BE downshift of Hf 4f and O 1 s (Table 2) for $\text{HfO}_x/\text{PVD-TiN}$ implies a larger magnitude of band bending. From the peak fitting results of Fig. 6, the E_{bb} results in Table 2 and Eq. (2), we deduce that the HfO_x layer in $\text{HfO}_x/\text{PVD-TiN}$ is more oxygen deficient than that of $\text{HfO}_x/\text{ALD-TiN}$ due to migration of a larger amount of O^{2-} interstitials to the PVD-TiN, which thus implies a higher N_d for $\text{HfO}_x/\text{PVD-TiN}$. This subsequently results in higher P_d - higher density of O^{2+} vacancies left in the dielectric HfO_x layer in $\text{HfO}_x/\text{PVD-TiN}$.

In Fig. 7c, the O 1 s peak shows a sudden increase in intensity at 1750 eV (the interface depth) for the $\text{HfO}_x/\text{PVD-TiN}$ sample. This opposes the general trend of decrease in intensity with increase in photon energy and indicates a large amount of oxygen content at the interface of the $\text{HfO}_x/\text{PVD-TiN}$ sample. This is consistent with the Ti 2p results seen in Fig. 5a where the increment in oxygen content at $\hbar\nu = 1750$ eV in Fig. 7c is ascribed to the formation of a thick interfacial TiO_2 layer between HfO_x and PVD-TiN. Also, at $\hbar\nu = 1250$ eV in Fig. 5a and 5b, Ti-O peaks are already visible in the Ti 2p spectra of both the $\text{HfO}_x/\text{PVD-TiN}$ and $\text{HfO}_x/\text{ALD-TiN}$ samples. Since Ti-O and Hf-O O 1 s peaks are very close in BE and cannot be resolved through peak fitting [42,43], peak fitting is thus not performed for the O 1 s and Hf 4f spectra specifically to calculate the ratio of O 1 s to Hf $4f_{7/2}$, except for those surface sensitive spectra obtained at low photon energies, as shown in Fig. 6.

Since the growth conditions of the HfO_2 ALD are kept the same for both samples, the composition differences of the final HfO_x layers must be due to the differences in the TiN BME. These can be mainly explained by (1) the differences in the crystal quality of ALD- and PVD-TiN; the differences might also perhaps be attributed to (2) the pristine ALD-TiN having a thicker TiO_2 overlayer, as compared to that of the PVD-TiN, which will be further elaborated in the next paragraph. The PVD-TiN is more defective than the ALD-TiN, as it has a smaller crystallite size and also possesses more grain boundaries, thereby creating more diffusion pathways for oxidation to take place when it was heated up to 200 °C during the HfO_2 ALD. Hence, more O^{2-} interstitials diffused from HfO_x into the PVD-TiN than into the ALD-TiN.

It is interesting to note that the TiO_2 interfacial layer is thicker for the $\text{HfO}_x/\text{PVD-TiN}$ than for $\text{HfO}_x/\text{ALD-TiN}$ (Fig. 5 and Fig. 7c-d), while the HfO_x layer closer to the surface is more oxygen-deficient in the $\text{HfO}_x/\text{PVD-TiN}$ sample (Fig. 6 and Table 1). Both can be attributed to stronger oxygen scavenging from the HfO_x layer in the $\text{HfO}_x/\text{PVD-TiN}$ sample. However, the pristine ALD-TiN reference sample has a thicker TiO_2 overlayer than the pristine PVD-TiN reference sample (Fig. 4a) prior to HfO_2 ALD. One should expect that the self-cleaning [11] of native oxide during HfO_2 ALD removed TiO_2 from both the PVD- and ALD-TiN BME with the same efficiency. There exists a possibility that when self-cleaning of native oxide (TiO_2) happened during the dosing of TEMA-Hf precursor in the HfO_2 ALD, part of the oxygen removed from the native oxide was re-absorbed back into the forming HfO_x layers at the same time [44] due to the more negative Gibbs free energy of formation of HfO_2 and higher oxygen affinity of HfO_2 . Since there was initially a slightly thicker TiO_2 overlayer on the pristine ALD-TiN (Fig. 4a), more dissociated oxygen from this dissipated layer would be absorbed into the forming HfO_x layer, if we assume complete removal of TiO_2 from the TiN

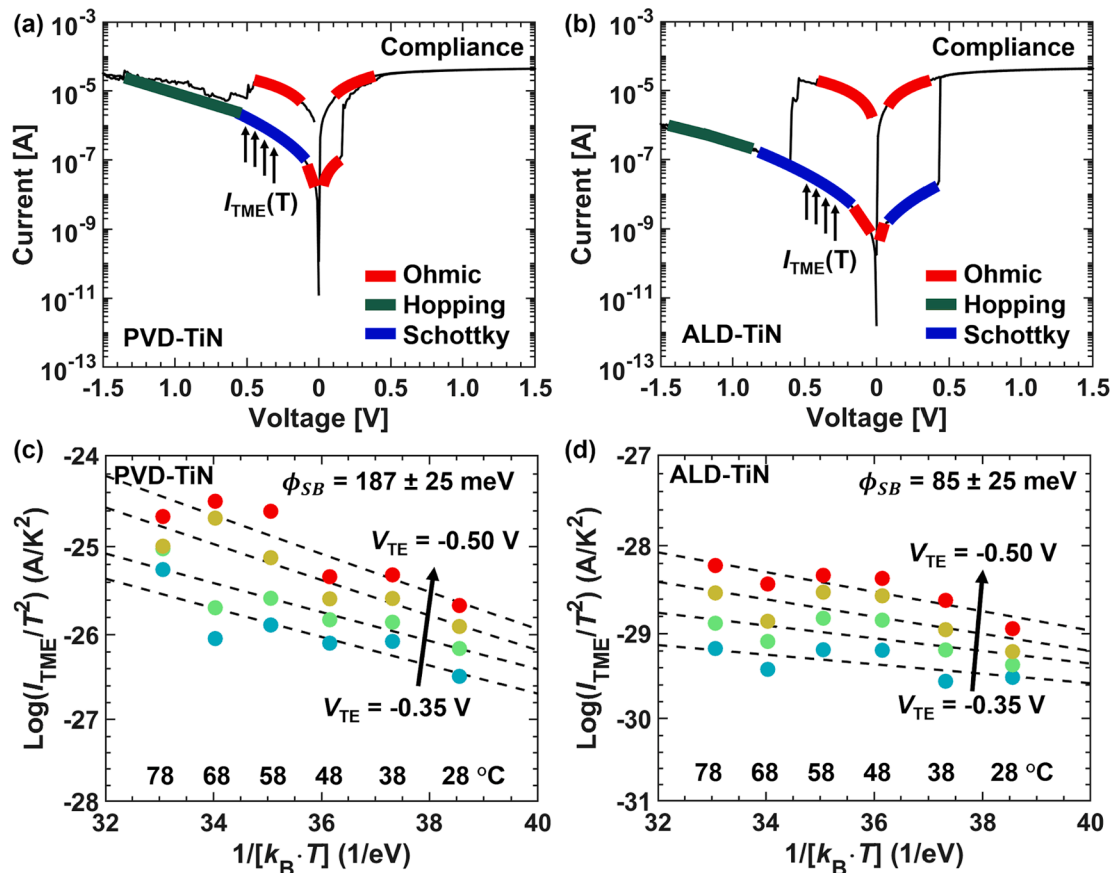


Fig. 8. Fitted graphs of DC switches show the type and regions of different conduction mechanisms in (a) PVD-TiN and (b) ALD-TiN devices. Richardson's graphs of (c) PVD-TiN and (d) ALD-TiN devices show the temperature dependence on the current measured between 28 °C and 78 °C in 10 °C steps. The PVD-TiN device has significantly larger temperature dependence, and the extracted barrier height is found to be more than twice as large as that of the ALD-TiN device.

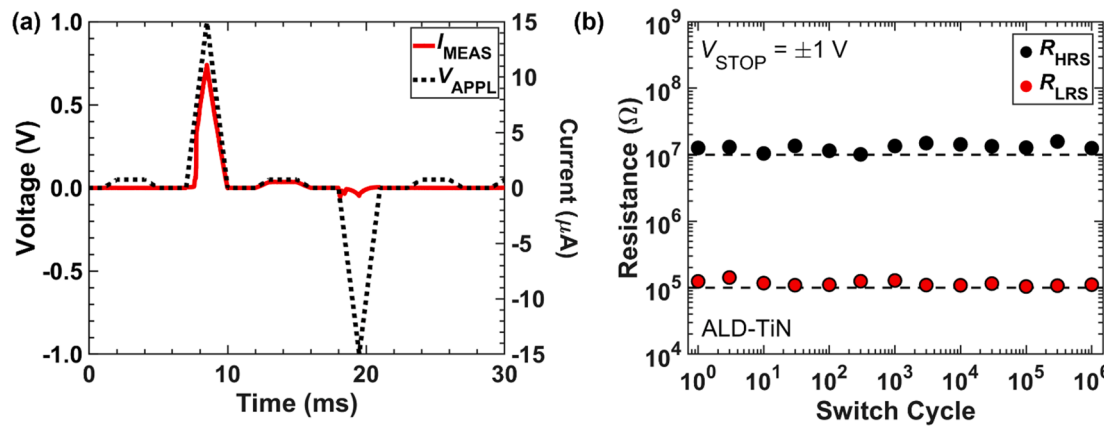


Fig. 9. (a) The ALD-TiN device was pulsed with ± 1 V, 3 ms pulses and a READ-SET-READ-RESET-READ sequence was shown. (b) A device was switched for 10^6 cycles, showing that consistent LRS and HRS values can be maintained.

BME upon HfO_x ALD. This will lead to less oxygen vacancies and thus a slightly higher oxygen content in the HfO_x layer of $\text{HfO}_x/\text{ALD-TiN}$, as compared to that of $\text{HfO}_x/\text{PVD-TiN}$. On the other hand, the stronger oxygen scavenging of the PVD-TiN layer would lead to an even more enhanced oxygen deficiency in the HfO_x layer of the $\text{HfO}_x/\text{PVD-TiN}$ sample. In both scenarios, we end up with a significantly more severe band bending situation in the HfO_x layer of the $\text{HfO}_x/\text{PVD-TiN}$, as compared to that of the $\text{HfO}_x/\text{ALD-TiN}$.

Since the electric field arising from the oxygen vacancies bends the energy bands of the HfO_x layer upward towards the interface, this situation indicates the presence of a Schottky barrier across the HfO_x/TiN interface, where the Schottky barrier height ϕ_{SB} should be proportional to the E_{bb} and thus to the density of oxygen vacancies (P_d) in the HfO_x layer.

3.4. Conduction behaviour analysis

To electrically verify the presence of a Schottky barrier at the HfO_x/TiN interface, fitting of different conduction modes was performed on DC switching characteristics as shown in Fig. 8a and 8b. Our fitted conduction mode regions are consistent with the fitting of other $\text{TiN}/\text{HfO}_x/\text{ITO}$ samples as reported in Ref. [45]. In the LRS at small biases, the conduction is Ohmic while in the HRS at intermediate voltages, the conduction changes to Schottky type, and then to Mott Gurney Hopping conduction at even higher voltages. While Schottky describes conduction over a barrier, hopping conduction is mitigated through trap to trap tunneling where the scattered oxygen vacancies in the region of the dissolved filament assist in the current conduction at higher fields. To estimate the ϕ_{SB} in the negative bias direction, the temperature dependent current at the TME, $I_{TME}(T)$, was measured at different temperatures in the HRS between -0.35 V to -0.50 V, as indicated by the arrows in Fig. 8a and 8b. The measurements are shown in the SM Fig. S7. By plotting the temperature data into Richardson's graphs, it is possible to extract the barrier height [46]. In Fig. 8c and 8d, ϕ_{SB} corresponds to about 187 meV and 85 meV for the PVD-TiN and the ALD-TiN devices, respectively. The temperature measurements confirm that the $\text{HfO}_x/\text{PVD-TiN}$ BME interface has a larger barrier.

3.5. Pulsed endurance

Finally, to evaluate the potential of the ALD-TiN OxRRAM, which showed narrower switching distributions, larger memory window, and higher margin for RFF, an endurance measurement was performed with 3 ms pulses where a READ, SET, READ, RESET, READ pulse train is displayed in Fig. 9a. The pulse width in the measurement is limited by the parasitic load attributed to the extrinsic 1T1R circuit. The measured device shows an endurance of 10^6 switches with an intact 100x memory

window for ± 1 V triangular pulses, as displayed in Fig. 9b. It is estimated that in a hybrid static RAM (SRAM) implementation, an endurance of 10^5 is sufficient to run deep learning applications for up to 10 years [47]. The same material stack as the ALD-TiN devices presented in this paper has also been evaluated on vertical III-V nanowires by Persson et al, demonstrating a similar endurance as well as a retention corresponding to 10 years at room temperature [3]. The paper also examined fast pulsing where sub-pJ switches are achievable with ± 1 V rectangular 50 ns pulses. With the potential of low power operation and with scalable, vertically integrated devices for reduced footprint, the investigated material stack is a promising candidate for future non-volatile memory solutions.

4. Conclusions

Via-RRAM devices with an etched-out TiN BME, lifting layer, and an ITO TME were fabricated alongside samples designated for XPS studies that consist of the same BME and HfO_x layers, but without any additional materials deposited. Two types of OxRRAM stacks were fabricated where the TiN BME was fabricated by physical vapor deposition (PVD) and atomic layer deposition (ALD), respectively. Electrical switching characteristics of OxRRAM devices show a large difference depending on the material properties of the BME. The larger reservoir of oxygen vacancies near the BME interface of the PVD-TiN OxRRAM devices effectively reduces the insulator thickness when forming in the positive direction. The reduced memory window and the gradual switching of the PVD-TiN OxRRAM devices might be mainly attributed to larger conductive filament base at the BME interface caused by the higher oxygen vacancy concentration near the BME interface. Relative to the ALD-TiN sample, the BME/oxide interface for the PVD-TiN has a larger concentration of oxygen vacancies, in turn increasing the probability for reverse filament growth during switching; this affects the RFF negatively, thereby compromising endurance with a reduced margin of failure. It also causes a larger filament base at the BME-oxide-interface, seemingly explaining the reduced memory window for the PVD-TiN device as compared to the ALD-TiN device due to the larger area of the ruptured filament surfaces.

The larger concentration of oxygen vacancies in the HfO_x layer of $\text{HfO}_x/\text{PVD-TiN}$ as compared to that of $\text{HfO}_x/\text{ALD-TiN}$ is revealed by SXPS. Our SXPS and the XRD results indicate that the HfO_x layer in $\text{HfO}_x/\text{PVD-TiN}$ is more oxygen deficient most likely because of (1) more defective PVD-TiN with smaller crystallite size and more grain boundaries, which lead to more oxygen interstitial scavenging from the HfO_x layer, and also possibly because (2) the pristine ALD-TiN has a thicker TiO_2 overlayer. Both the O 1 s and Hf 4f peaks shift to lower BE with increased proximity to the HfO_x/TiN interface in both samples because of upward band bending of the energy bands in the HfO_x layer. The HfO_x

layer in $\text{HfO}_x/\text{PVD-TiN}$ exhibit a larger magnitude of the band bending due to its greater oxygen deficiency. The oxygen vacancy-induced band bending in the HfO_x layer comes along with a Schottky barrier formed at the HfO_x/TiN interface. The Schottky barrier height was obtained from electrical transport measurements as 187 ± 25 meV for the $\text{HfO}_x/\text{PVD-TiN}$ sample and only 85 ± 25 meV for the $\text{HfO}_x/\text{ALD-TiN}$ sample, in agreement with the strong difference in band bending between both samples obtained by SXPS. The larger required switching voltages for the PVD-TiN device are possibly caused by a combination of the larger filament base and a larger Schottky barrier.

Our RRAM devices implementing 3.3 nm-thick ultra-scaled- HfO_x and ALD-TiN BME show promising performance with intact low voltage switching up to 10^6 cycles with ± 1.0 V and $10 \mu\text{A}$ programming pulses. Furthermore, our in-depth studies of the oxide/BME interface demonstrate how a combined electrical and physico-chemical characterization can reveal the material properties that are the reason behind several improved or degraded RRAM switching properties, thus leading the path towards a more effective and characterization-driven development of future RRAM devices.

Declaration of Competing Interest

The authors declare that they have no known competing financial interests or personal relationships that could have appeared to influence the work reported in this paper.

Acknowledgements

This work was performed within the NanoLund Center for Nanoscience and was further supported by the Swedish Research Council, grant nos. 2014-04580, 2016-06186, 2017-03871, and 2017-04108. We also acknowledge the funding support from The Knut and Alice Wallenberg Foundation. The authors want to acknowledge Mattia Scardamaglia, Suyun Zhu, and Andrey Shavorskiy (MAX IV) for experimental support and Alexei Preobrajenski (MAX IV) for helpful discussions.

Appendix A. Supplementary data

Supplementary data to this article can be found online at <https://doi.org/10.1016/j.apsusc.2021.149386>.

References

- [1] A. Chen, A review of emerging non-volatile memory (NVM) technologies and applications, *Solid-State Electronics* 125 (2016) 25–38.
- [2] Z. Jiang, S. Qin, H. Li, S. Fujii, D. Lee, S. Wong, H.-S.P. Wong, Next-Generation Ultrahigh-Density 3-D Vertical Resistive Switching Memory (VRSM)—Part II: Design Guidelines for Device, Array, and Architecture, *IEEE Transactions on Electron Devices* 66 (2019) 5147–5154.
- [3] K.M. Persson, M.S. Ram, O.P. Kilpi, M. Borg, L.E. Wernersson, Cross-Point Arrays with Low-Power ITO-HfO₂ Resistive Memory Cells Integrated on Vertical III-V Nanowires, *Advanced Electronic Materials* (2020) 2000154.
- [4] M.S. Ram, K.-M. Persson, M. Borg, L.-E. Wernersson, Low-Power Resistive Memory Integrated on III-V Vertical Nanowire MOSFETs on Silicon, *IEEE Electron Device Letters* (2020).
- [5] C.-W. Hsu, I.-T. Wang, C.-L. Lo, M.-C. Chiang, W.-Y. Jang, C.-H. Lin, T.-H. Hou, Self-rectifying bipolar Tao x, TiO₂ RRAM with superior endurance over 10 12 cycles for 3D high-density storage-class memory, in:, *Symposium on VLSI Technology*, IEEE 2013 (2013) T166–T167.
- [6] C.-C. Lin, P.-H. Chen, M.-C. Chen, T.-C. Chang, C.-Y. Lin, H.-X. Zheng, C.-K. Chen, W.-C. Huang, W.-C. Chen, H.-C. Huang, Investigating Material Changes at Different Gadolinium Doping Power Levels in Indium-Tin Oxide Intended for Use as an Insulator in Resistive Switching Memory, *IEEE Transactions on Electron Devices* 66 (2019) 2595–2599.
- [7] S. Balatti, S. Ambrogio, Z.-Q. Wang, S. Sills, A. Calderoni, N. Ramaswamy, D. Ielmini, Understanding pulsed-cycling variability and endurance in HfO_x RRAM, in: 2015 IEEE International Reliability Physics Symposium, IEEE, 2015, pp. 5B. 3.1–5B. 3.6.
- [8] J.-W. Yoon, J.H. Yoon, J.-H. Lee, C.S. Hwang, Impedance spectroscopic analysis on effects of partial oxidation of TiN bottom electrode and microstructure of amorphous and crystalline HfO₂ thin films on their bipolar resistive switching, *Nanoscale* 6 (2014) 6668–6678.
- [9] S. Brivio, J. Frascari, S. Spiga, Role of metal-oxide interfaces in the multiple resistance switching regimes of Pt/HfO₂/TiN devices, *Applied Physics Letters* 107 (2015), 023504.
- [10] C. Hinkle, E. Vogel, P.D. Ye, R. Wallace, Interfacial chemistry of oxides on In_xGa (1-x) As and implications for MOSFET applications, *Current Opinion in Solid State and Materials Science* 15 (2011) 188–207.
- [11] R. Timm, A.R. Head, S. Yngman, J.V. Knutsson, M. Hjort, S.R. McKibbin, A. Troian, O. Persson, S. Urpelainen, J. Knudsen, Self-cleaning and surface chemical reactions during hafnium dioxide atomic layer deposition on indium arsenide, *Nature communications* 9 (2018) 1–9.
- [12] M. Sowinska, T. Bertaud, D. Walczyk, S. Thiess, M.A. Schubert, M. Lukosius, W. Drube, C. Walczyk, T. Schroeder, Hard x-ray photoelectron spectroscopy study of the electroforming in Ti/HfO₂-based resistive switching structures, *Applied Physics Letters* 100 (2012), 233509.
- [13] R. Nyholm, J. Andersen, U. Johansson, B. Jensen, I. Lindau, Beamline I311 at MAX-LAB: a VUV/soft X-ray undulator beamline for high resolution electron spectroscopy, *Nuclear Instruments and Methods in Physics Research Section A: Accelerators, Spectrometers, Detectors and Associated Equipment* 467 (2001) 520–524.
- [14] J. Park, J. Woo, A. Prakash, S. Lee, S. Lim, H. Hwang, Improved reset breakdown strength in a HfO_x-based resistive memory by introducing RuO_x oxygen diffusion barrier, *AIP Advances* 6 (2016), 055114.
- [15] S. Balatti, S. Ambrogio, Z.-Q. Wang, S. Sills, A. Calderoni, N. Ramaswamy, D. Ielmini, Pulsed cycling operation and endurance failure of metal-oxide resistive (RRAM), in: 2014 IEEE International Electron Devices Meeting, IEEE, 2014, pp. 14.13. 11-14.13. 14.
- [16] K.-M. Persson, M.S. Ram, M. Borg, L.-E. Wernersson, Investigation of reverse filament formation in ito, hfo₂-based rram, in:, *Device Research Conference (DRC)*, IEEE 2019 (2019) 91–92.
- [17] D. Berco, T.-Y. Tseng, A numerical analysis of progressive and abrupt reset in conductive bridging RRAM, *Journal of Computational Electronics* 15 (2016) 586–594.
- [18] D. Ielmini, V. Milo, Physics-based modeling approaches of resistive switching devices for memory and in-memory computing applications, *Journal of Computational Electronics* 16 (2017) 1121–1143.
- [19] Z. Yong, J. Linghu, S. Xi, H.R. Tan, L. Shen, P. Yang, H.K. Hui, J.Q. Cao, M.L. Leek, X. Yin, Ti_{1-x}Sn_xO₂ nanofilms: Layer-by-layer deposition with extended Sn solubility and characterization, *Applied Surface Science* 428 (2018) 710–717.
- [20] G. Greczynski, L. Hultman, Self-consistent modelling of X-ray photoelectron spectra from air-exposed polycrystalline TiN thin films, *Applied Surface Science* 387 (2016) 294–300.
- [21] G. Greczynski, L. Hultman, In-situ observation of self-cleansing phenomena during ultra-high vacuum anneal of transition metal nitride thin films: Prospects for non-destructive photoelectron spectroscopy, *Applied Physics Letters* 109 (2016), 211602.
- [22] S. Logothetidis, E. Meletis, G. Stergioudis, A. Adjaottor, Room temperature oxidation behavior of TiN thin films, *Thin Solid Films* 338 (1999) 304–313.
- [23] H.-Y. Chen, F.-H. Lu, Oxidation behavior of titanium nitride films, *Journal of Vacuum Science & Technology A: Vacuum, Surfaces, and Films* 23 (2005) 1006–1009.
- [24] J. Desmaison, P. Lefort, M. Billy, Oxidation mechanism of titanium nitride in oxygen, *Oxidation of Metals* 13 (1979) 505–517.
- [25] M. Wittmer, J. Noser, H. Melchior, Oxidation kinetics of TiN thin films, *Journal of Applied Physics* 52 (1981) 6659–6664.
- [26] B.E. Deal, A. Grove, General relationship for the thermal oxidation of silicon, *Journal of Applied Physics* 36 (1965) 3770–3778.
- [27] H.G. Tompkins, Oxidation of titanium nitride in room air and in dry O₂, *Journal of Applied Physics* 70 (1991) 3876–3880.
- [28] H.-D. Kim, M.J. Yun, S.M. Hong, J.H. Park, D.S. Jeon, T.G. Kim, Impact of roughness of bottom electrodes on the resistive switching properties of platinum/nickel nitride/nickel 1 × 1 crossbar array resistive random access memory cells, *Microelectronic engineering* 126 (2014) 169–172.
- [29] K. Egorov, R. Kirtaev, Y.Y. Lebedinskii, A. Markeev, Y.A. Matveyev, O. Orlov, A. Zablotskiy, A. Zenkevich, Complementary and bipolar regimes of resistive switching in TiN/HfO₂/TiN stacks grown by atomic-layer deposition, *physica status solidi (a)* 212 (2015) 809–816.
- [30] L. Ye, T. Gougousi, Diffusion and interface evolution during the atomic layer deposition of TiO₂ on GaAs (100) and InAs (100) surfaces, *Journal of Vacuum Science & Technology A: Vacuum, Surfaces, and Films* 34 (2016) 01A105.
- [31] D.-Y. Cho, Band alignments in oxygen-deficient HfO₂/Si (100) interfaces, *Journal of Korean Physical Society* 51 (2007) 647.
- [32] P. Cakir, R. Eloirdi, F. Huber, R.J. Konings, T. Gouder, An XPS and UPS Study on the Electronic Structure of ThO_x ($x \leq 2$) Thin Films, *The Journal of Physical Chemistry C* 118 (2014) 24497–24503.
- [33] H. Chang, M. Liang, Oxygen vacancy estimation of high k metal gate using thermal dynamic model, *Applied Physics Letters* 97 (2010), 041912.
- [34] S.R. Bradley, K.P. McKenna, A.L. Shluger, The behaviour of oxygen at metal electrodes in HfO₂ based resistive switching devices, *Microelectronic engineering* 109 (2013) 346–350.
- [35] K.P. McKenna, Structure, electronic properties, and oxygen incorporation/diffusion characteristics of the Σ 5 TiN (310)[001] tilt grain boundary, *Journal of Applied Physics* 123 (2018), 075301.
- [36] S. Guha, V. Narayanan, High-k/metal gate science and technology, *Annual Review of Materials Research* 39 (2009) 181–202.
- [37] S. Guha, V. Narayanan, Oxygen vacancies in high dielectric constant oxide-semiconductor films, *Physical review letters* 98 (2007), 196101.

- [38] A.S. Foster, F.L. Gejo, A. Shluger, R.M. Nieminen, Vacancy and interstitial defects in hafnia, *Physical Review B* 65 (2002), 174117.
- [39] J. Gavartin, D. Muñoz Ramo, A. Shluger, G. Bersuker, B. Lee, Negative oxygen vacancies in Hf O₂ as charge traps in high-k stacks, *Applied Physics Letters* 89 (2006), 082908.
- [40] F. Ji-Bin, L. Hong-Xia, G. Bo, M. Fei, Z. Qing-Qing, H. Yue, Influence of different oxidants on the band alignment of HfO₂ films deposited by atomic layer deposition, *Chinese Physics B* 21 (2012), 087702.
- [41] X. Wang, K. Han, W. Wang, J. Xiang, H. Yang, J. Zhang, X. Ma, C. Zhao, D. Chen, T. Ye, Band alignment of HfO₂ on SiO₂/Si structure, *Applied Physics Letters* 100 (2012), 122907.
- [42] H. Hernandez-Arriaga, E. Lopez-Luna, E. Martínez-Guerra, M. Turrubiarres, A. Rodriguez, M. Vidal, Growth of HfO₂/TiO₂ nanolaminates by atomic layer deposition and HfO₂-TiO₂ by atomic partial layer deposition, *Journal of Applied Physics* 121 (2017), 064302.
- [43] Y. Xiong, X. Chen, F. Wei, J. Du, H. Zhao, Z. Tang, B. Tang, W. Wang, J. Yan, Electrical Properties of Ultrathin Hf-Ti-O Higher k Gate Dielectric Films and Their Application in ETSOI MOSFET, *Nanoscale research letters* 11 (2016) 533.
- [44] G. D'Acunto, A. Troian, E. Kokkonen, F. Rehman, Y.-P. Liu, S. Yngman, Z. Yong, S. R. McKibbin, T. Gallo, E. Lind, Atomic Layer Deposition of Hafnium Oxide on InAs: Insight from Time-Resolved *In Situ* Studies, *ACS Applied Electronic Materials* 2 (2020) 3915–3922.
- [45] P.-H. Chen, K.-C. Chang, T.-C. Chang, T.-M. Tsai, C.-H. Pan, C.-Y. Lin, F.-Y. Jin, M.-C. Chen, H.-C. Huang, M.-H. Wang, Improving performance by doping gadolinium into the indium-tin-oxide electrode in HfO₂-based resistive random access memory, *IEEE Electron Device Letters* 37 (2016) 584–587.
- [46] L. Michalas, A. Khiat, S. Stathopoulos, T. Prodromakis, Electrical characteristics of interfacial barriers at metal–TiO₂ contacts, *Journal of Physics D: Applied Physics* 51 (2018), 425101.
- [47] A. Grossi, E. Vianello, M.M. Sabry, M. Barlas, L. Grenouillet, J. Coignus, E. Beigne, T. Wu, B.Q. Le, M.K. Wootters, Resistive RAM endurance: Array-level characterization and correction techniques targeting deep learning applications, *IEEE Transactions on Electron Devices* 66 (2019) 1281–1288.